Water wave transmission by an array of floating disks.

L. G. Bennetts[1] and T. D. Williams[2]

[1]School of Mathematical Sciences, University of Adelaide, Adelaide 5005, Australia

[2]Nansen Environment and Remote Sensing Centre, Bergen 5006, Norway

September 16, 2014

Abstract

An experimental validation of theoretical models of regular-water-wave transmission through arrays of floating disks is presented. The experiments were conducted in a wave basin. The models are based on combined potential-flow and thin-plate theories, and the assumption of linear motions. A low-concentration array, in which disks are separated by approximately a disk diameter in equilibrium, and a high-concentration array, in which adjacent disks are almost touching in equilibrium, were used for the experiments. The proportion of incident-wave energy transmitted by the disks is presented as a function of wave period, and for different wave amplitudes. Results indicate the models predict wave-energy transmission accurately for small-amplitude waves and low-concentration arrays. Discrepancies for large-amplitude waves and high-concentration arrays are attributed to wave overwash of the disks and collisions between disks. Validation of model predictions of a solitary disk's rigid-body motions are also presented.

1   Introduction

Theoretical models of water-wave transmission by large groups of floating, thin plates have been developed for over forty years now. The models are based on wave-scattering theories. They are used to predict attenuation rates of ocean-surface waves in the ice-covered ocean, noting alternative theories to model waves in the ice-covered ocean also exist (e.g. Weber, 1987; Keller, 1998; Wang and Shen, 2010). The component models of wave scattering by solitary plates are extensions of models developed in other areas of hydrodynamics (e.g. Linton and McIver, 2001). Wave interactions between plates are calculated using modified versions of methods developed to model acoustic and electromagnetic waves (e.g. Ishimaru, 1978; Martin, 2006).

Transmission models, however, have not been thoroughly validated via experimental data. The lack of validation is conspicuous now that attenuation models are being integrated into large-scale operational forecasting and climate models (Perrie and Hu, 1996; Doble and Bidlot, 2013; Williams et al., 2013a,b).

Squire and Moore (1980) and Wadhams et al. (1988) used measurements of waves in the ice-covered ocean to provide evidence wave energy attenuates approximately exponentially with respect to distance travelled. Further, the measurements indicate attenuation rates depend on wave period. In particular, the ice cover acts as a low-pass filter, i.e. long-period waves maintain energy for the greatest distance into the ice-covered ocean.

Wadhams (1973, 1986) developed the first theoretical model of wave attenuation due to ice cover. The model is two-dimensional, with one horizontal dimension and one depth dimension, i.e. one-dimensional surface waves. Potential-flow theory is used to model water motions. Linear motions are assumed. The ice cover is modelled as a collection of floating, thin-elastic plates. (Elastic plates are conventionally used to model sea ice.) Attenuation results from an accumulation of scattering events. Wave energy is not removed from the overall system. The scattering events themselves are due to

impedance mismatches when a wave travels between a region of open water and a region in which a plate covers the water surface.

Wadhams (1973, 1986) applied a single-scattering approximation. The proportion of wave energy transmitted by multiple plates is, thus, the product of wave-energy proportions transmitted by the plates individually. The model, therefore, predicts exponential attenuation, at a rate proportional to $\ln(T)$, where T is the proportion of energy transmitted by a solitary plate.

Stoker (1957, § 10) solved the problem of wave transmission by a solitary, thin-elastic plate in shallow water. Wadhams (1973, 1986) was only able to approximate the energy transmitted in the extended, deep-water problem (and hence the attenuation rate) crudely. Meylan and Squire (1994) later developed a method to calculate the full-linear solution for scattering by a solitary, thin-elastic plate in deep water, and thus, in principle, obtain the attenuation rate predicted by the model of Wadhams (1973, 1986).

Kohout and Meylan (2008) extended the model of Wadhams (1973, 1986) to include multiple wave scatterings, i.e. multiple reflections and transmissions between plates. In the multiple-scattering model, unlike the single-scattering model, transmission by an individual realisation of the plates depends on their configuration. Disorder in plate locations and properties results in exponential attenuation of wave energy with distance travelled. Kohout and Meylan (2008) applied a Monte Carlo algorithm with respect to randomly generated realisations of the plates to calculate a mean attenuation rate for a given wave period and average properties of the plates.

Bennetts and Squire (2012a,b) developed a similar model to Kohout and Meylan (2008), but in which wave phases between plates are considered to be random variables, and the attenuation rate, rather than the transmitted energy, is averaged. They produced an analytic solution for the attenuation rate predicted by the model, in terms of the energy transmitted by a solitary plate, under the assumption only travelling waves interact between adjacent plates — the so-called wide-spacing approximation. The resulting attenuation rate is identical to that predicted by the model of Wadhams (1973, 1986) due to wave decoherence, as explained by Berry and Klein (1997).

The linear potential-flow/thin-plate model has been extended to three dimensions, i.e. two-dimensional surface waves. The plates are commonly assumed to be disks. Peter and Meylan (2004), for example, proposed a solution method for a finite number of floating, thin-elastic plates, using Graf's interaction theory (Abramowitz and Stegun, 1964). The method is, however, in practice, limited to O(100) plates by computational costs. Bennetts et al. (2010) developed a three-dimensional model for an infinite field of plates. The solution method, however, relied on imposition of an artificial periodicity in one horizontal dimension, following methods developed to model electromagnetic wave scattering (e.g. Botten et al., 2004).

Meylan et al. (1997) proposed a model of wave-energy transport through an array of randomly distributed, identical disks, by combining the potential-flow/thin-plate model for an individual disk (Meylan and Squire, 1996) with wave-energy-transport theory (Ishimaru, 1978). Meylan and Masson (2006) showed the transport theory used by Meylan et al. (1997) is almost identical to the transport theory developed by Masson and LeBlond (1989). Masson and LeBlond (1989)'s transport theory was based on an approximate solution of the two-dimensional wave equation, using the Foldy (1945) closure assumption and the single-scattering approximation. Masson and LeBlond (1989) also modelled the component disks as being rigid, using the solution method outlined by Isaacson (1982).

Kohout and Meylan (2008), Bennetts et al. (2010) and Bennetts and Squire (2012b) compared attenuation rates predicted by their respective models to attenuation rates extracted from field data, which were reported by Squire and Moore (1980) and Wadhams et al. (1988). The comparisons indicate broadly reasonable model/data agreement for mid-range wave periods (6 s to 15 s estimated by Kohout and Meylan, 2008). However, the comparisons are far from comprehensive in terms of the properties of the ice cover and wave field. Notably, the experimental data lacks information on incident wave amplitudes.

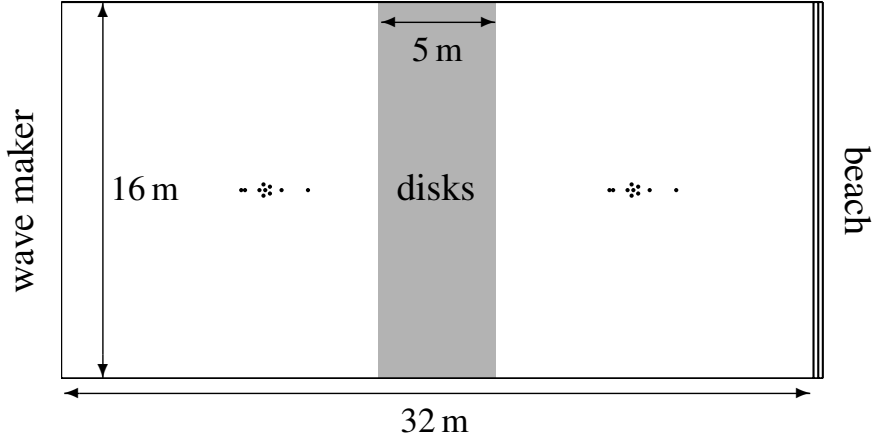Results of a laboratory, experimental campaign to study transmission of regular water waves by

Figure 1: Schematic plan view of wave basin. Dots indicate wave probe locations. Ambient fluid depth is 3.1 m.

τ_{tg} [s]	0.65	0.8	0.8	0.95	0.95	1.1	1.25	1.25	1.4	1.4	1.55	1.7	1.85	2	2
A_{tg} [mm]	10	10	20	15	30	20	20	40	20	40	20	20	20	20	50
$c = 0.38$	•			•	•		•	•			•		•		
$c = 0.77$	•	•	•	•		•	•		•	•	•	•	•	•	•

Table 1: Summary of tests conducted, with respect to target wave period, τ_{tg}, amplitude, A_{tg}, and concentration, c.

large arrays of floating disks are reported here. The results are compared to predictions given by the models of Wadhams (1973, 1986)/Bennetts and Squire (2012a,b) and Meylan et al. (1997)/Meylan and Masson (2006). The investigation represents, to the authors' knowledge, the first experimental validation of the models, as models of water-wave transmission by an array of floating disks, as opposed to models of wave attenuation in the ice-covered ocean.

The investigation also contains the first validation of rigid-body motions of a solitary disk in response to wave forcing, as predicted by the models. Montiel et al. (2013b,a) provided the only previous related validation. However, Montiel et al. (2013b,a) applied artificial restraints to the disk to match the model assumptions, as part of the experimental set-up. In particular, a rod was used to restrict surge motions, and a barrier was attached to the edge of the disk to prevent wave overwash.

The model-data comparisons presented here indicate linear potential-flow/thin-plate and transport theories predict wave transmission accurately for small incident wave amplitudes and low disk concentrations. For large incident wave amplitudes and high concentrations the wave energy transmitted in the experiments is significantly less that that predicted by the models. The discrepancies are attributed to the unmodelled dissipative processes of wave overwash of the disks and collisions between disks.

2 Experimental design

The experimental campaign was conducted using the Basin de Génie Océanique FIRST wave basin facility, located at Océanide, La Seyne sur Mer, France. The wave basin is 32 m long, bounded at one end by a unidirectional wave maker and at the opposite end by a static beach. The basin is 16 m wide, bounded by reflective walls. The ambient fluid depth in the basin was set at $h = 3.1$ m. Figure 1
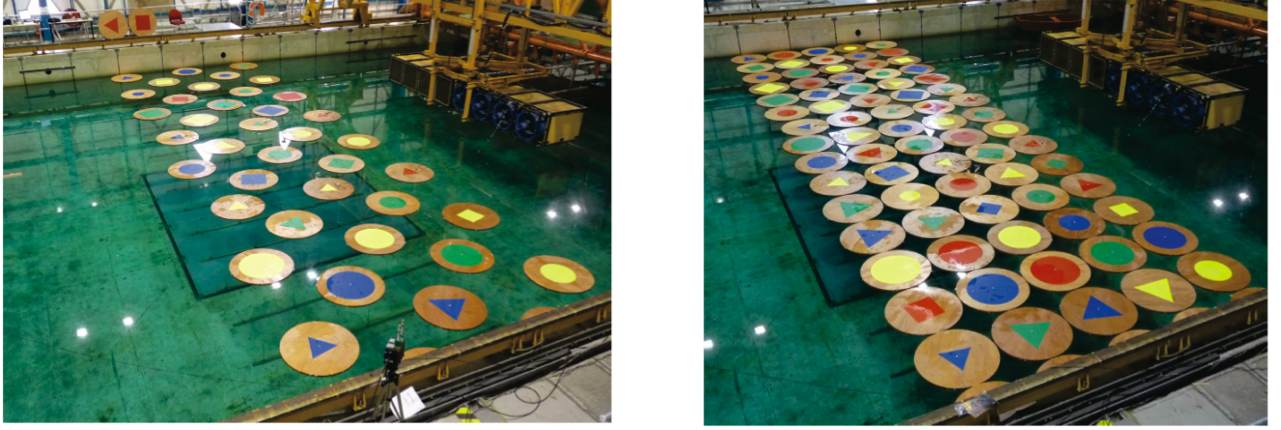
Figure 2: Photos of disk arrays: low concentration (left-hand panel) and high concentration (right).

shows a schematic plan view of the wave basin.

Wooden disks were installed in the wave basin. The disks have radius $a = 0.495\,\mathrm{m}$ and thickness $D = 33\,\mathrm{mm}$. The disks have mass of approximately $14\,\mathrm{kg}$, and a draught of $d = 18\,\mathrm{mm}$. The Young's modulus of the wood used for the disks was measured as $E = 4\,\mathrm{GPa}$, using a cantilevered beam. The disks are, therefore, approximately rigid.

Each disk was loosely moored to the basin floor. The mooring system consisted of a series of three springs and a steel cable. The natural period of the moored disks was measured as $\tau_\mathrm{m} = 12.5\,\mathrm{s}$, which is at least an order of magnitude greater than the wave periods used. The mooring, therefore, permitted the disks to respond naturally in rigid-body motions to wave forcing, but returned the disks to the same initial locations for each test.

Low- and high-concentration arrays of the disks were considered. Eighty disks were used for the high-concentration array. The centres of the disks formed a rectangular lattice of $1\,\mathrm{m}$ by $1\,\mathrm{m}$ squares, with five rows and sixteen columns, i.e. adjacent disks almost touching in equilibrium. The equilibrium concentration of the disks on the water surface was approximately $c = 0.77$. The low-concentration array was formed by removing alternate disks from the high-concentration array. The equilibrium concentration in this case was approximately $c = 0.38$. Figure 2 shows photos of the two arrays.

Regular incident waves of a prescribed target period, τ_tg, and target amplitude, A_tg, were generated by the wave maker. Two groups of probes were used to measure the incident wave-field before the disks and the transmitted wave-field after the disks. Figure 1 indicates the location of the probes. The groups consist of (i) a line of probes in the direction of the incident wave, and (ii) a pentagon of probes, to analyse the directional spectrum of the waves (not considered here, see §4.3). The probes have an accuracy of at least $1\,\mathrm{mm}$, and a sampling frequency of $250\,\mathrm{Hz}$.

Target wave periods used for the tests were in the range $0.65\,\mathrm{s}$ to $2\,\mathrm{s}$. Target wave amplitudes of $10\,\mathrm{mm}$, $15\,\mathrm{mm}$ and $20\,\mathrm{mm}$ were used for wave periods $0.65\,\mathrm{s}$ to $0.8\,\mathrm{s}$, $0.95\,\mathrm{s}$ and $1.1\,\mathrm{s}$ to $2\,\mathrm{s}$, respectively. Larger wave amplitudes were also used for selected wave periods. For all period/amplitude combinations the wave steepness was less than $5\,\%$ to avoid wave breaking. Table 1 provides a summary of the tests conducted. A subset of the tests were repeated.

Accelerometers were attached to six of the disks. Four of the accelerometers were triaxial and two were biaxial, in the plane of the disk surface. The six chosen disks comprised two disks from the front row, two from the middle row and two from the back row. The disks were in the off-centre columns, and hence formed two lines of three disks.

Tests were also conducted for a solitary disk. The target periods and amplitudes used for the single-disk tests were identical to those used for the low-concentration array tests. The Krypton motion-tracking system was used to record the six rigid-body motions of the disk during the tests.

Quantity	Symbol	Value
Disk thickness	D	$33\,\mathrm{mm}$
Disk radius	a	$0.495\,\mathrm{m}$
Disk draught	d	$18\,\mathrm{mm}$
Disk Young's modulus	E	$4\,\mathrm{GPa}$
Disk Poisson's ratio	ν	0.3
Water depth	h	$3.1\,\mathrm{m}$
Water density	ρ	$1025\,\mathrm{kg\,m^{-3}}$

Table 2: Disk and water properties used in model calculations.

Three light-emitting diodes (LEDs) were attached to the disk. The LEDs were monitored by a camera, mounted on a platform approximately two metres away from the disk. The Krypton system constructs time series of translational and rotational motions of the disk from the coordinates of the LEDs. The translations have a maximum error of $1\,\mathrm{mm}$, and the rotations 0.1 degree.

3   Theoretical model

3.1   Preliminaries

A Cartesian coordinate system (x, y, z) is used to define positions in the water, where (x, y) is the horizontal coordinate and z is the vertical coordinate. The incident wave travels in the x-direction. The vertical coordinate points upwards and has its origin set to coincide with the undisturbed free surface of the water.

The models are based on potential-flow theory for water motions. Thus, the water is assumed to be homogeneous, incompressible, inviscid and in irrotational motion. It follows that the velocity field can be defined as the gradient of a velocity potential, $\Phi(x, y, z, t)$. Time-harmonic motions, of prescribed period, τ, and angular frequency $\omega = 2\pi/\tau$, are assumed. The velocity potential is, therefore, expressed as $\Phi(x, y, z, t) = \mathrm{Re}\{(g/\mathrm{i}\omega)\phi(x, y, z)\mathrm{e}^{-\mathrm{i}\omega t}\}$. Here $\phi(x, y, z)$ is a (reduced) velocity potential and $g \approx 9.81\,\mathrm{m\,s^{-2}}$ is acceleration due to gravity.

The incident wave steepness is assumed to be sufficiently small that linear theory models motions accurately. Linear theory reduces the problem from the unknown, moving domain to the fixed, equilibrium domain, assuming the moving domain is a perturbation from the equilibrium domain. The linearised velocity potential satisfies Laplace's equation throughout the undisturbed water domain, i.e.

$$\nabla^2 \phi = 0 \qquad (-h < z < z_0), \tag{1}$$

where $z_0 = 0$ and $-d$ in the free-surface and disk-covered water regions, respectively. An impermeability boundary condition is applied at the basin floor, i.e. $\partial_z \phi = 0$ $(z = -h)$.

The water surface elevation is expressed as $z = z_0 + \zeta(x, y, t) = z_0 + \mathrm{Re}\{\eta(x, y)\mathrm{e}^{-\mathrm{i}\omega t}\}$, where $\eta(x, y)$ is the (reduced) surface elevation. It is assumed the lower surfaces of the disks remain in contact with the water surface beneath at all points and at all times during motion. In the disk-covered regions the surface elevation, therefore, represents the displacement of the disk-water interface. The surface elevation and velocity potential are coupled via the kinematic condition $\partial_z \phi = \sigma\eta$ $(z = z_0)$, where $\sigma = \omega^2/g$ is a frequency parameter.

The surface elevation and velocity potential are also coupled via a dynamic condition. In free-surface regions, the dynamic condition is derived by applying the linear Bernoulli equation at the equilibrium water surface and assuming a constant atmospheric pressure. The dynamic condition is simply $\phi = \eta$ $(z = 0)$.

The equations of motion for the disks in the vertical direction are used to derive the dynamic condition in the disk-covered regions. Following the majority of models referenced in § 1, Kirchhoff-

Love thin-plate theory is used to model the disks. Kirchhoff-Love theory assumes small displacements, and, hence, plate motions can be obtained from the displacements of their lower surfaces, η. The resulting dynamic condition is

$$(1 - \sigma d)\eta + F\nabla^4\eta = \sigma\phi \quad (z = -d) \qquad \text{where} \qquad F = \frac{ED^3}{12\rho g(1 - \nu^2)}, \tag{2}$$

is a scaled flexural rigidity of the disk, $\rho \approx 1025\,\text{kg}\,\text{m}^{-3}$ is water density, and $\nu \approx 0.3$ is Poisson's ratio. (Disk and water properties used in the model are summarised in table 2.)

Free-edge conditions are also applied to the disks, which ensure bending moments and shearing stresses vanish. The free-edge conditions are

$$\nabla^2\eta - (1 - \nu)\left(\partial_s^2\eta + \kappa\partial_n\eta\right) = 0 \qquad \text{and} \qquad \partial_n\nabla^2\eta + (1 - \nu)\partial_s\partial_n\partial_s\eta = 0, \tag{3}$$

for $(x, y) \in \Gamma = \{(x, y) : x^2 + y^2 = a^2\}$, where κ is curvature of the circular boundary, and ∂_n and ∂_s are the normal and tangential derivatives, respectively.

Note the above governing equations for a floating Kirchhoff-Love plate reduce to those for a heaving and pitching, floating, rigid plate in the large-rigidity limit, up to linear terms in thickness. Eatock-Taylor (2007) relates the equations for a floating Kirchhoff-Love plate to those of a floating, rigid plate.

The model permits hydrodynamic pressure on the submerged portions of the disk edges, caused by wave motion, to force the disks to surge back and forth at the frequency of the incident wave. The location of the centre of a disk, which, without loss of generality, has its equilibrium centre set to coincide with the origin of the horizontal coordinate system, is hence $(x, y) = (\text{Re}\{Xe^{-i\omega t}\}, 0)$. The surge amplitude, X, is coupled to the velocity potential via dynamic and kinematic conditions applied on the equilibrium locations of the submerged portions of the disk edges, again assuming the moving interface is a small perturbation away. The conditions are

$$\partial_x\phi = \sigma X \quad ((x, y) \in \Gamma, -d < z < 0) \qquad \text{and} \qquad -\sigma d\pi a^2 X = \int_\Gamma \int_{-d}^0 [\phi]_{(x,y)\in\Gamma} \, \mathrm{d}z \, \mathrm{d}s. \tag{4}$$

The model does not include motions in the y-direction (sway, roll and yaw) excited by scattered waves, as they are assumed not to affect the transmitted waves on average.

3.2 Transmission models

3.2.1 Two-dimensional model

A simplified, two-dimensional model is derived by neglecting motions in the y-direction, and using a geometry that is representative of a cross section in the (x, z) plane. Each individual disk then partially reflects and partially transmits incident waves. Reflection and transmission properties of individual disks are combined to calculate reflection and transmission properties of the group of disks.

Two models are considered here. First, a model in which a single-scattering approximation is applied (Wadhams, 1973, 1986). Second, a model in which multiple wave reflections and transmissions are included (Bennetts and Squire, 2012a,b). In the latter, wave phases between disks are considered to be random variables, and the energy transmitted by a group of disks is calculated as an average over all possible phases between disks. The models do not require disk locations to be specified.

Both models predict the energy transmitted by the group of disks to be $T^{cL/a}A_{\text{tg}}^2$, where T is the proportion of energy transmitted by a solitary disk of radius $a = 0.495\,\text{m}$, draught $d = 18\,\text{mm}$ and Young's modulus $E = 4\,\text{GPa}$ for wave period τ_{tg}. The quantity $L = 5\,\text{m}$ is the distance travelled by the wave. Note that the two-dimensional model predicts the logarithm of the transmitted energy is proportional to the concentration of the disks, c.

3.2.2 Wave energy transport model

Meylan et al. (1997) and Meylan and Masson (2006) developed a model of wave-energy transport through a region of floating disks, using the potential-flow/thin-plate model of an individual disk for the scattering kernel. The transport model considers the directional spectrum of average wave energy with respect to random realisations of disk locations, denoted S. The underlying transport theory is heuristic, i.e. it is not based on the governing equations outlined in § 3.1 or any other fundamental wave equation (Ishimaru, 1978). However, Howells (1960), for example, shows a transport equation can be derived from the wave equation, assuming the single-scattering approximation.

Here, the average wave energy is assumed to be independent of location across the basin width, i.e. no wall effects, and to represent the steady regime, i.e. independent of time. Thus, $S = S(x, \theta)$, where θ is an angle, measured with respect to the positive x-axis, denoting wave direction. Setting the disk-covered region to occupy the interval $0 < x < L$, the transport model in the present setting is

$$\cos(\theta)\partial_x S(x, \theta) = \frac{c}{\pi a^2} \int_{-\pi}^{\pi} K(\theta - \hat{\theta}) S(x, \hat{\theta}) \, \mathrm{d}\hat{\theta} - qS(x, \theta) \qquad (0 < x < L), \tag{5}$$

where K is the scattering kernel for the given disk properties and wave period τ_{tg}. The left-hand side of equation (5) provides steady advection of the wave spectrum. The right-hand side provides scattering of wave energy. The integral represents wave energy scattered in direction θ by all other directions, $\hat{\theta}$. The term $qS(x, \theta)$ represents wave energy in direction θ scattered into all other directions, i.e.

$$q = \frac{c}{\pi a^2} \int_{-\pi}^{\pi} K(\hat{\theta}) \, \mathrm{d}\hat{\theta}. \tag{6}$$

Incident wave energy from the wave-maker side of the disks is specified by the boundary conditions

$$S(0, \theta) = \frac{1}{2} A_{\mathrm{tg}}^2 \delta(\theta) \quad (|\theta| < \pi/2) \qquad \text{and} \qquad S(L, \theta) = 0 \quad (|\theta| > \pi/2), \tag{7}$$

where δ denotes the Delta function. (Note that incident wave energy has been normalised to half the incident-amplitude-squared.) The wave energy spectrum, S, is calculated using a discretisation of the angular coordinate, θ, and applying a generalised spectral method to the resulting system of ordinary differential equations (Meylan et al., 1997; Meylan and Masson, 2006).

4 Results

4.1 Data processing

A short-time Fourier transform (STFT, e.g. Allen and Rabiner, 1977) method is used to convert raw time series of surface elevations, and disk translations and rotations into spectral representations of amplitudes in time, i.e. spectrograms. Representative amplitudes for chosen wave periods and time intervals are extracted from the spectrograms.

For a given time series, amplitudes are calculated using the following algorithm.

1. The series is windowed. A target window width is specified. The actual window width used is that closest to the target width, which contains a power of two samples.

2. The inverse fast Fourier transform is applied to the series in each window, and the (generalised) wave energies in the associated frequency bins calculated.

3. The energy at the target period, $E_{\mathrm{tg}}(\hat{t})$, is calculated as the sum of the energy in the bin containing that period, and energies contained in up to three bins either side of that bin. Here $\hat{t}$ denotes mean time for the window. The corresponding amplitude is $\sqrt{2E_{\mathrm{tg}}}$.
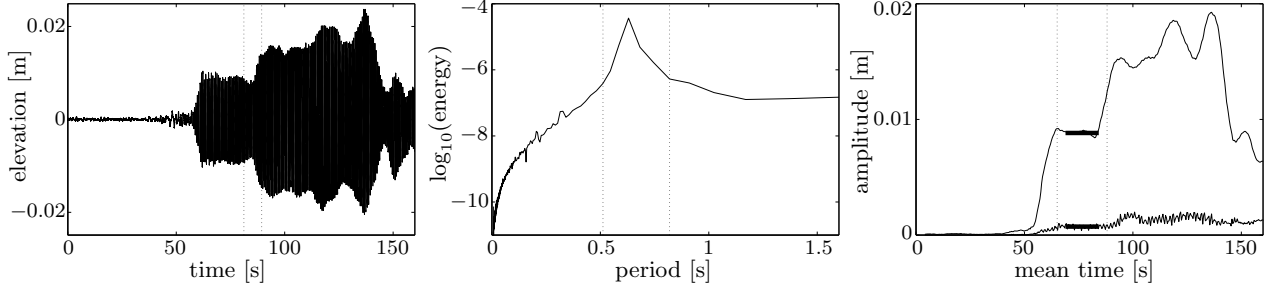
Figure 3: Example conversion of time series to representative amplitude in steady-state interval. Left-hand panel shows raw-surface-elevation time series from probe closest to wave maker, for test with target wave period 0.65 s and high-concentration array. Dotted vertical lines indicate a time window. Middle panel shows the energy spectrum for the indicated window. Dotted vertical lines indicate bins used to calculate the amplitude at the target period. Right-hand panel shows the amplitude at the target period and half the target period (smaller) as functions of mean time. Dotted vertical lines indicate the steady-state interval. Bars indicate the extracted amplitude and chosen interval.

4. A time interval of interest is defined. Typically, a steady-state interval is selected. The steady-state interval begins after transients in the leading waves have passed, and ends before the signal is contaminated by reflections from geometrical boundaries. A representative amplitude for the interval of interest is calculated as the mean of the amplitudes in the interval.

Figure 3 shows an example of conversion from time series to amplitudes. The left-hand panel shows a single window on the raw time series. Window width is chosen to balance time localisation (narrow windows) and spectral resolution (wide windows, see, e.g., Cohen, 1989). The target width in the example shown is ten target wave periods. (Target widths are three wave periods for the largest target wave periods.)

The middle panel shows the energy spectrum in the example window. A peak around the target wave period, $\tau_{\mathrm{tg}} = 0.65$ s, is evident. Spectral leakage is also evident.

The right-hand panel shows amplitudes of the target wave period and half the target period, i.e. the first and second harmonics, as functions of mean time. The steady-state interval is also indicated. In the case considered, the lower bound of the interval is the time at which the incident waves reach the probe, and the upper bound is the time at which the first waves reflected by the disks reach the probe. The interval is calculated analytically via the group velocity. The amplitudes vary near to the boundaries of the interval, which is partially due to smearing produced by the STFT method. (The chosen example shows particularly strong variation.) Representative amplitudes are, therefore, extracted from a smaller interval. In this case, the interval is the middle two-thirds of the full steady-state interval.

4.2 Solitary disk: response amplitude operators

Let time series of disk translations in the x- and z-directions be denoted $\mathcal{X}(t)$ and $\mathcal{Z}(t)$, respectively, and the angle of rotation of the surface about the y-axis be denoted $\Psi(t)$. In the steady-state interval the translational and rotational motions are

$$\mathcal{X} \approx \mathrm{Re}\{X_d \mathrm{e}^{-2\pi \mathrm{i} t/\tau_{\mathrm{m}}} + X \mathrm{e}^{-2\pi \mathrm{i} t/\tau_{\mathrm{tg}}}\}, \quad \mathcal{Z} \approx \mathrm{Re}\{Z \mathrm{e}^{-2\pi \mathrm{i} t/\tau_{\mathrm{tg}}}\} \quad \text{and} \quad \Psi \approx \mathrm{Re}\{\psi \mathrm{e}^{-2\pi \mathrm{i} t/\tau_{\mathrm{tg}}}\}. \tag{8}$$

The quantity X_d is the amplitude of the long-period disk motion related to the mooring system, which is excited by drift forces. Drift is not analysed here. Moreover, the time-harmonic models used do not include the drift/mooring motion, assuming the long-period motion ($\tau_{\mathrm{m}} = 12.5$ s $\gg \tau_{\mathrm{tg}}$) does not affect motions at the target period. The quantities X and Z are, respectively, the amplitudes of surge
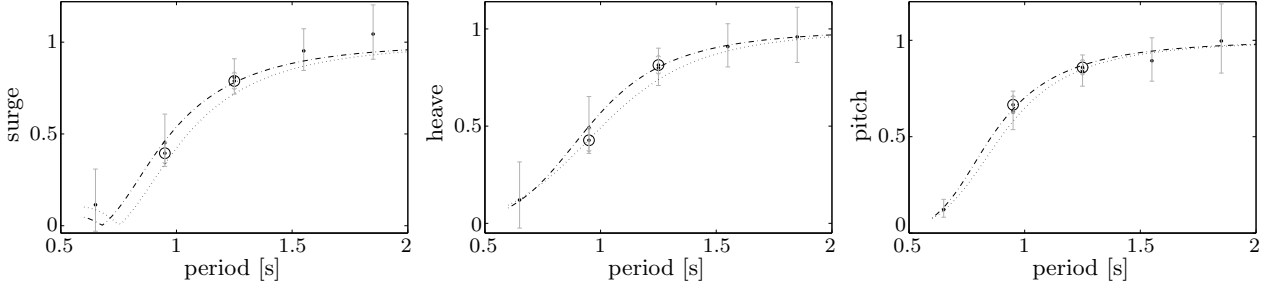
8

Figure 4: RAOs for a solitary disk. Bullets denote experimental data. Encircled bullets denote data from large-amplitude tests. Grey bars denote error bounds from measuring devices. Curves denote results of theoretical models. Dotted curves are results from the two-dimensional model and chained curves are results from the disk model.

Figure 5: Example of onset of overwash with increased wave amplitude. Photos are of solitary-disk tests for target wave period $0.95\,\mathrm{s}$ and amplitudes $15\,\mathrm{mm}$ (left-hand panel) and $30\,\mathrm{mm}$ (right).

and heave motions of the disk. The quantity ψ is the amplitude of angle of rotation about the y-axis, and is the arctangent of the amplitude of pitch motion of the disk. The amplitudes X, Z and ψ are extracted from time series for $\mathcal{X}$, $\mathcal{Z}$ and Ψ using the algorithm described in § 4.1. (Note, the algorithm filters out the long-period oscillations associated with the drift/mooring.)

The amplitude of surge motion is calculated explicitly in the theoretical models. Amplitudes of heave and pitch motions are obtained from the displacement function, η, via

$$Z = \frac{1}{\pi a^2} \iint_\Omega \eta(x,y) \ \mathrm{d}x\mathrm{d}y \quad \text{and} \quad \tan(\psi) = \frac{1}{4\pi a^4} \iint_\Omega x\eta(x,y) \ \mathrm{d}x\mathrm{d}y, \tag{9}$$

for the disk model, where Ω is the lower surface of the disk. Analogous expressions exist for the two-dimensional model.

The response amplitude operators (RAOs) are normalised to tend to unity in the long-period limit, in which the disk does not affect the incident wave. The RAOs associated to surge, heave and pitch motions are, therefore, $\sigma|X|/(kA)$, $|Z|/A$ and $|\tan(\psi)|/(kA)$, respectively. The wavenumber, k, is the positive real root of the dispersion relation $k\tanh(kh) = \sigma$. The amplitude of the incident wave, A, for a given test, is calculated as the mean amplitude in the steady-state intervals of the time series given by the ten probes on the wave-maker side of the disk, prior to arrival of reflected waves. The incident wave amplitude is $A = A_{\mathrm{tg}}$ in the models.

Figure 4 shows a comparison of the RAOs calculated from the experimental data and the theoretical models. Error bounds for the experimental data are obtained by adding/subtracting the maximum errors in the measuring devices from the calculated translations, rotations and incident wave amplitudes.

The mean difference between the model predictions and data over wave periods and the three RAOs is 4.87×10^{-2} for the two-dimensional model and 3.01×10^{-2} for the disk model. Agreement is,
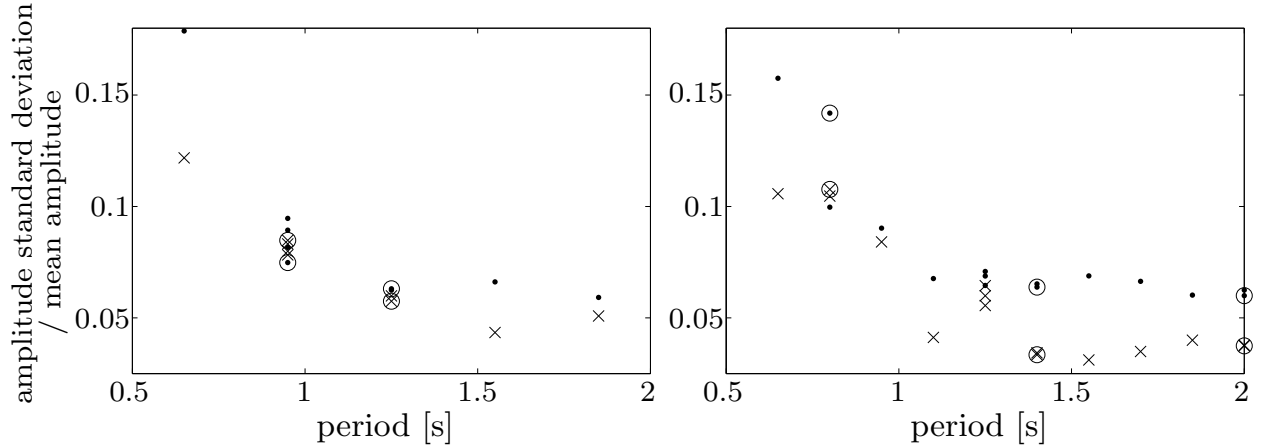
Figure 6: Standard deviations in wave amplitudes scaled with respect to mean amplitudes for low-concentration array tests (left-hand panel) and high-concentration array tests (right). Dots denote transmitted waves. Crosses denote incident waves. Circles denote large-amplitude tests.

therefore, marginally better for the disk model than the two-dimensional model. Agreement is also best for heave, with mean difference 4.78×10^{-3} for the disk model.

The two models, themselves, are similar over the chosen range of wave periods. The two-dimensional model, however, tends to suppress motions in comparison to the disk model.

Tests using wave periods $0.95\,\mathrm{s}$ and $1.25\,\mathrm{s}$ were conducted for two wave amplitudes. In both cases, the larger amplitude was twice the smaller amplitude. For tests using wave period $1.25\,\mathrm{s}$, the two amplitudes produce RAOs with a relative difference of approximately $2.22\,\%$, averaged over the RAOs. For tests using wave period $0.95\,\mathrm{s}$, the two amplitudes produce RAOs with a relative difference approximately $10.6\,\%$, which is slightly under five times larger than the difference in the $1.25\,\mathrm{s}$ wave period test. Note, the larger amplitude reduces the translational, surge and heave RAOs and increases the rotational, pitch RAO for the $0.95\,\mathrm{s}$ wave period.

Wave overwash of the disk is a visible effect of increasing amplitude. Overwash refers to the wave running over the top of the disk. It is not included in models. Overwash provides an explanation of the change in the RAOs for the large-amplitude test using a wave period $0.95\,\mathrm{s}$. Translational motions are suppressed by the extra load of the overwashed fluid on the disk surface. Conversely, pitch motions are enhanced, as rotations force front and back ends of the disk (with respect to the incident wave) to be submerged alternately. Overwashed water originates from the submergences.

Figure 5 shows photos of the disk in the tests using wave period $0.95\,\mathrm{s}$. Full overwash is evident for the large-amplitude test. For the instant captured by the photo, the angle of rotation of the disk is maximal with respect to the negative x-axis. Overwashed water is, therefore, generated at the back end of the disk in this phase of its motion. Only a small quantity of water is visible on the disk surface for the small-amplitude test. Overwash also occured during the large-amplitude test using wave period $1.25\,\mathrm{s}$, and the test using wave period $0.65\,\mathrm{s}$. However, in both cases, the overwash was weaker, in terms of depth and disk coverage, than in the large-amplitude test using wave period $0.95\,\mathrm{s}$.

4.3 Multiple disks: wave transmission

The transmitted wave-fields were dominated, visibly, by a plane wave in the incident-wave direction for all tests, except those using the smallest wave period, $\tau_{\mathrm{tg}} = 0.65\,\mathrm{s}$. (In comparison, the reflected wave-fields, which are not analysed here, were often short-crested.) Geometrically decaying circular wave-fields emanating from the back row of disks were, however, also visible for tests using wave
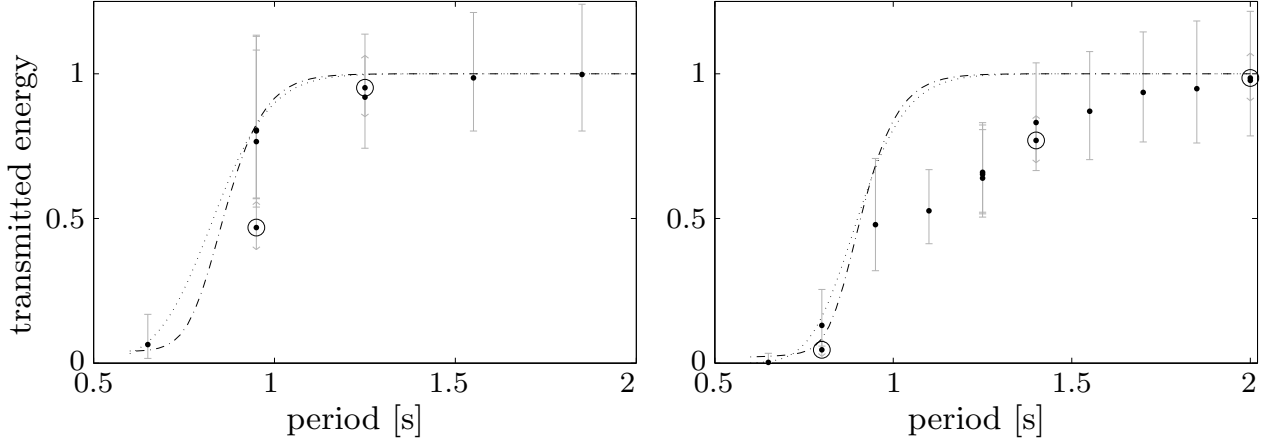
Figure 7: Transmitted energy proportion for low-concentration array tests (left-hand panel) and high-concentration array tests (right). Curves and symbols as in figure 4.
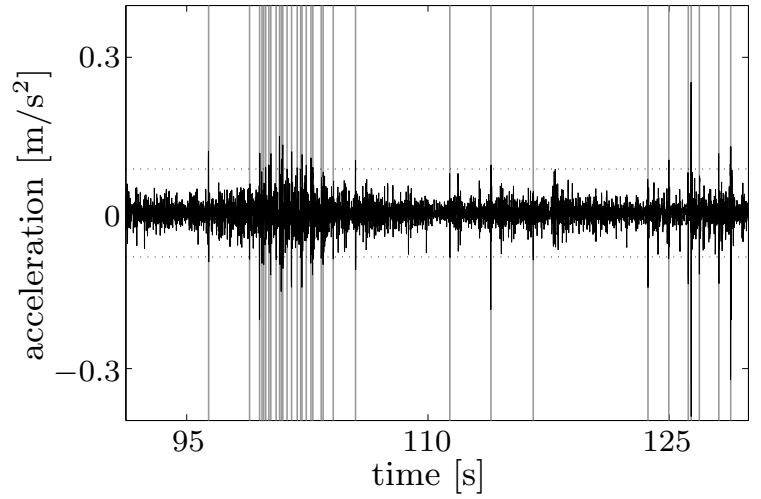

Figure 8: Photo at time 100 s of subset of disks in a high-concentration array test, centred around disks with accelerometers in right-of-centre column of full array, using target wave period 0.65 s and amplitude 10 mm (left-hand panel), and high-pass-filtered acceleration time series for disk in middle row (right). Thresholds of collisions (black-dotted, horizontal lines) and locations of collisions (grey, vertical lines) are overlaid on acceleration time series.
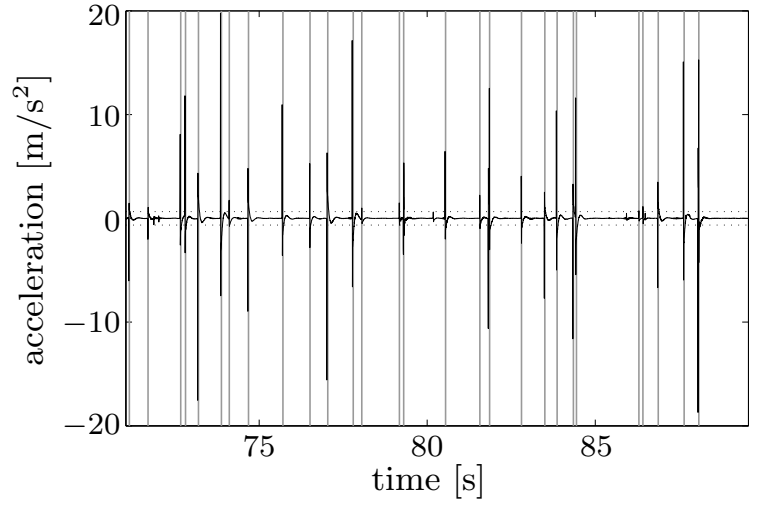
Figure 9: As in figure 8 but for test using target wave period 1.25 s and amplitude 20 mm. Photo taken at time 74 s.
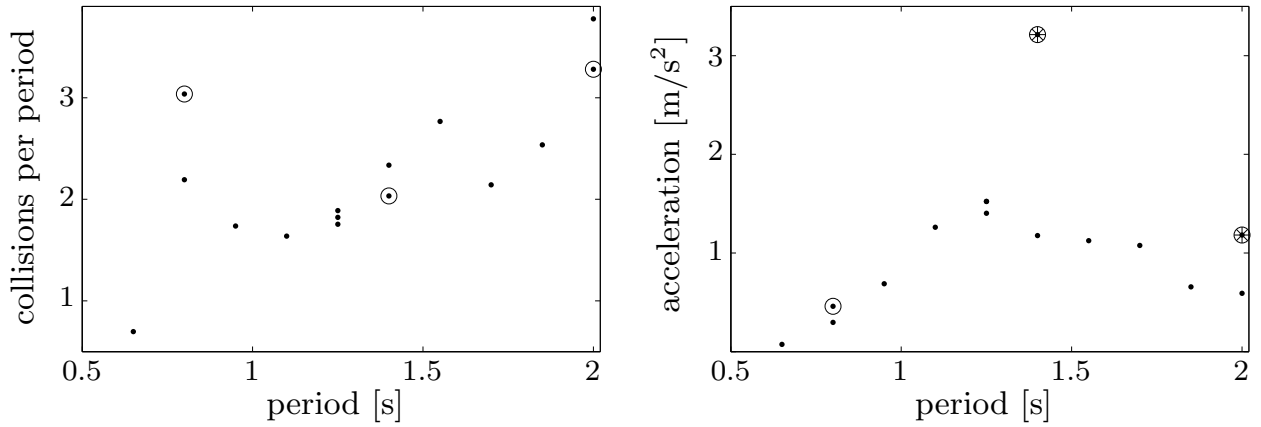

Figure 10: Mean number of collisions experienced by disks with accelerometers in middle row of high-concentration array per target wave period (left-hand panel), and corresponding mean magnitude of accelerations (right). Asterisks denotes tests in which one or more collisions saturates the signal.
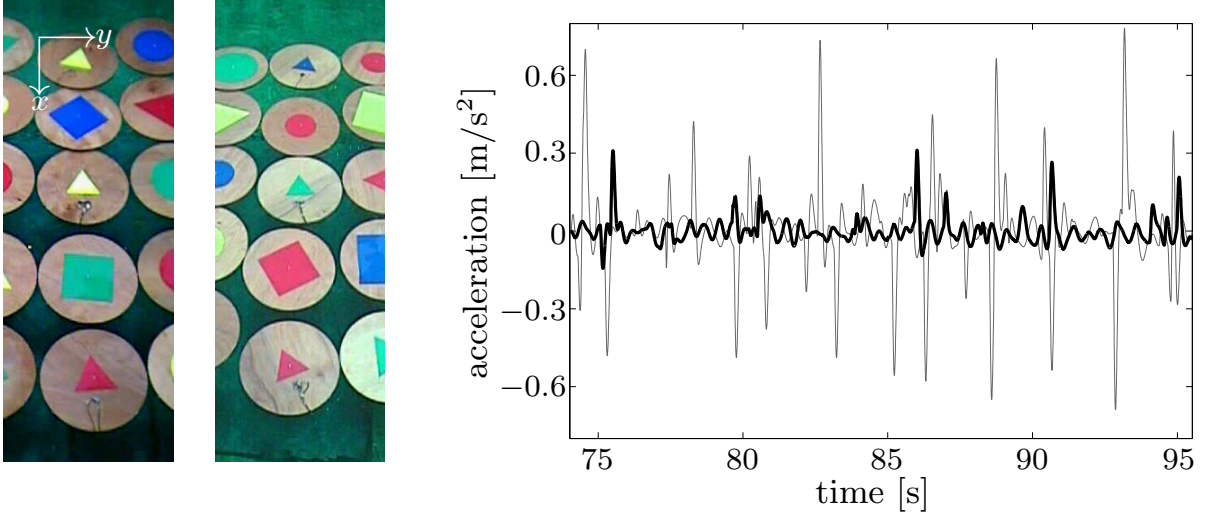
Figure 11: Example of rafting event in test using target wave period 1.1 s and amplitude 20mm. Left-hand photo shows disks in left-of-centre column, with three top disks rafted, and right-hand photo shows right-of-centre column, with no disks rafted. Right-hand panel shows low-pass-filtered response of accelerometers in middle of left column (black curve) and right column (grey).

periods less than or equal to 1.25 s. A transmitted wave amplitude, A_T, is, therefore, calculated from the experimental data as the mean of the amplitudes in the steady-state intervals of the time series given by the ten probes on the beach side of the disks.

Figure 6 shows the standard deviations in transmitted amplitudes over the array of probes, scaled with respect to the corresponding mean amplitude. Scaled standard deviations are also shown for the incident waves, i.e. amplitudes from the probes on the wave-maker side of the array. Standard deviations are less than 10 % of their corresponding mean amplitudes for all tests, except those using the smallest wave period, $\tau_{\text{tg}} = 0.65$ s, and the large-amplitude test using wave period 0.8 s for the high-concentration array. The small standard deviations support the observation of plane-wave dominance of transmitted wave-fields at the probes in the majority of the tests, as a directional wave spectrum would produce spatial variations in wave amplitude.

Further, standard-deviation-to-mean ratios are almost identical to their incident-wave counterparts for the low-concentration tests, indicating variations in the transmitted wave-field are due to imperfections in the incident waves. The exception is the test using wave period 0.65 s. For tests using the high-concentration array, standard-deviation-to-mean ratios are appreciably larger for the transmitted wave-fields than the incident wave-fields, by up to a factor of approximately 2.2. The standard deviations, therefore, indicate the high-concentration array produces some directional components in the transmitted wave-field, which were not observed visually.

Standard deviations of transmitted amplitudes for tests in which plane-wave dominance was not visible were less than 0.5 mm, i.e. beneath the resolution of the wave probes. Analysis of the directional spectrum of the transmitted wave-fields is, therefore, not conducted here.

The proportion of energy transmitted by the disks is calculated as $(A_T/A)^2$. The two-dimensional model predicts the transmitted energy $(A_T/A)^2 = (A_T/A_{\text{tg}})^2 = T^{cL/a}$. For the transport model, the transmitted energy is calculated as the energy contained in the transmitted wave spectrum in a small band around the incident wave angle, i.e.

$$A_T^2 = 2 \int_{-\theta_0}^{\theta_0} S(L, \theta) \, \mathrm{d}\theta. \tag{10}$$

The band width parameter is $\theta_0 = \pi/40$ in the results presented.

13

Figure 7 shows a comparison of the proportion of energy transmitted by the disks, calculated from the experimental data and the theoretical models. The incident amplitude, A, is calculated from the experimental data, in this case, as the mean steady-state amplitude given by the ten probes on the beach side of the disks in tests conducted without the array of disks. The method is chosen to account for small attenuation of waves simply in travelling from the wave maker to the probes. Error bounds for the experimental data are obtained as for the RAOs.

The two-dimensional and transport models give almost identical predictions of the transmitted energy in the chosen interval of wave periods. Both predict monotonic increase in transmission as wave period increases. Small differences between the predictions are evident for wave periods approximately less than $1.25\,\mathrm{s}$. The transmitted energies interleave one another in the intervals that they differ. Consequently, there is no clear characteristic behavioural difference for transmission between the models.

The models capture the proportion of energy transmitted by the low-concentration array with a mean difference of 4.19×10^{-2} from the experimental measurement. The mean is calculated over all tests, except the large-amplitude test using wave period $0.95\,\mathrm{s}$. The mean difference for this test is 2.42×10^{-1}, i.e. an order of magnitude greater than the other tests. This is a consequence of significant amplitude dependence for tests using wave period $0.95\,\mathrm{s}$. The increase in amplitude from $15\,\mathrm{mm}$ to $30\,\mathrm{mm}$ causes the transmitted energy to reduce by approximately $40\,\%$. The effect of increasing amplitude found here for multiple disks is far more pronounced than for the RAOs of a solitary disk seen in §4.2, as may be anticipated. The amplitude dependence again coincides with strong overwash. For the large-amplitude test, all disks were overwashed, despite attenuation of the wave amplitude with distance travelled through the array.

In comparison, the increase in amplitude from $20\,\mathrm{mm}$ to $40\,\mathrm{mm}$ for tests using wave period $1.25\,\mathrm{s}$ produces a very small increase in the transmitted energy, which is within the bounds of uncertainty. All disks were overwashed in the large-amplitude test. However, as in the corresponding solitary-disk test, the overwash was weak. The results indicate weak overwash has a negligible effect on wave-energy transmission.

The models and data both indicate the high-concentration array transmits less wave energy than the low-concentration array. However, the mean difference between the models and data is 1.65×10^{-1} for the high-concentration array tests, which is approximately an order of magnitude greater than the small-amplitude tests for the low-concentration array. The models and data differ least for wave periods less than $0.95\,\mathrm{s}$, where strong attenuation occurs, and for the largest wave period, $\tau_{\mathrm{tg}} = 2\,\mathrm{s}$, for which the incident wave is fully transmitted.

Amplitude dependence is evident for the tests using wave period $0.8\,\mathrm{s}$. Here, increasing the amplitude from $10\,\mathrm{mm}$ to $20\,\mathrm{mm}$ results in the proportion of wave energy transmitted being reduced by approximately $65\,\%$. However, the impact of the reduction is debatable due to strong attenuation of the small-amplitude wave. Moreover, it is difficult to state whether the models agree more closely with the small- or large-amplitude test.

Amplitude dependence is also evident for tests using wave period $1.4\,\mathrm{s}$. However, the dependence is weak. Increasing the amplitude from $20\,\mathrm{mm}$ to $40\,\mathrm{mm}$ results in wave-energy transmission being reduced by approximately $7\,\%$.

The models and data differ most for tests using wave periods in the mid-range interval $0.95\,\mathrm{s}$ to $1.85\,\mathrm{s}$. The experimental data indicates less energy is transmitted than the models. In particular, the models predict full transmission for periods greater than approximately $1.6\,\mathrm{s}$, whereas the experimental data indicates some energy attenuation occurs for all periods tested. Differences are greatest for periods $1.1\,\mathrm{s}$, $1.25\,\mathrm{s}$ and $1.4\,\mathrm{s}$ (large amplitude), with the models overestimating transmission approximately $81\,\%$, $53\,\%$ and $30\,\%$, respectively.

Discrepancies between models and data for mid-range wave periods cannot be attributed simply to extrapolation of small discrepancies for tests using the low-concentration array to tests using the high-concentration array. Disk collisions are a probable source of additional wave-energy attenuation

in the high-concentration tests. Adjacent disks are separated by approximately 10 mm in the high-concentration tests, which makes the disks susceptible to collisions under wave forcing. Collisions did not occur in the low-concentration tests. Attenuation due to collisions is not included in the models.

The strength and frequency of collisions during the tests are quantified here to support the hypothesis that collisions are the primary source of discrepancy between models and data. Data provided by the accelerometers initially in the x-direction, i.e. the direction of the incident waves, are used to identify collisions and quantify their strength. Collision data are considered for the two disks equipped with accelerometers in the middle row to minimise influence of the mooring system on collisions properties presented.

Collisions are detected using the following algorithm.

1. The steady-state intervals of the acceleration time series are identified, as for the wave probes.

2. A third-order Butterworth filter is used to separate the high- and low-frequency components of the series.

3. Thresholds of two times the significant accelerations of the low-pass-filtered time series, i.e. four standard deviations, are set.

4. Collisions are identified as accelerations in the high-pass-filtered time series with magnitudes greater than or equal to the thresholds. (Collisions occurring repeatedly for up to ten consecutive time steps are regarded as the same collision, i.e. collisions are allowed a duration of 0.04 s.)

Figures 8 and 9 show two examples of the algorithm, along with corresponding snapshots of a subset of the disks.

Figure 10 shows the mean number of collisions experienced by the disks per wave period, and the mean magnitude of the accelerations caused by the collisions. Accelerations occasionally exceeded $2g$ in two tests, which saturated the signals. The mean accelerations calculated, thus, slightly underestimate the true mean.

Collisions occurred approximately once per wave period for the test using wave period 0.65 s and amplitude 10 mm. Surge amplitudes were not large enough to cause collisions in this test. Collisions were, rather, caused by out-of-phase pitch motions of adjacent disks in the same column of the array. However, the collisions were very weak, and did not force collided disks to separate. Thus, the initial configuration of the array was approximately maintained during the test, as shown in the left-hand panel of figure 8.

Collisions occurred more than three times per period for the tests using a 2 s wave period. Surge amplitudes of the disks were largest in these tests. However, adjacent disks surged almost exactly in phase with one another. Small differences in the phase of surge motions caused disks to collide, but, typically, weakly.

Collisions occurred approximately twice per wave period for mid-range periods. In the mid-range regime the collisions were at their strongest, as surge amplitudes and phase differences were large simultaneously. Strong collisions caused collided disks to rebound and collide with the opposing disk. Hence, two collisions tended to occur in quick succession. This behaviour can be inferred from the right-hand panel of figure 9.

The strength of collisions in the tests using wave period 1.4 s are amplitude dependent. Increasing the amplitude from 20 mm to 40 mm results in mean accelerations increasing by at least a factor 2.7. (The true factor is unknown as the accelerations saturated the signal for the large-amplitude test.) Weak dependence of energy transmission on wave amplitude for tests using wave period 1.4 s is, therefore, attributed to dependence of collision strength on wave amplitude.

It is noted that collisions can turn into rafting events when (i) relative motions of the disks allow for non-planar overlapping of edges, and (ii) the collisions are not so strong as to cause disks to separate due to a glancing collision. Rafting events occurred in three tests, with respective wave periods and

amplitudes 0.8 s and 40 mm, 0.95 s and 30 mm, and 1.1 s and 40 mm. Rafting events tend to develop in chains. Chains of up to four disks were created in the tests conducted.

Figure 11 shows an example of a rafting event. The disk in the middle row and left-of-centre column is rafted for almost the full duration of the steady-state window, starting at 76 s and lasting beyond 96 s. The corresponding disk in the right-of-centre column is not rafted during the steady-state window. The low-pass-filtered acceleration time series for the two disks indicates rafting suppresses the motion of the disk. Rafting also reduces the number of collisions experienced by the disk. The rafted disk experienced 22 collisions in the steady-state window, compared to 42 collisions experienced by the disk that did not raft. However, no clear relationship is found here between rafting events and wave-energy transmission.

5   Summary and discussion

Results of the first experimental campaign to investigate transmission of regular water waves by arrays of floating disks in a wave basin have been reported. The disks were wooden, with radius 0.495 m and thickness 33 mm. A low-concentration array, consisting of 40 disks, and a high-concentration array, consisting of 80 disks, were considered. Wave periods in the range 0.65 s to 2 s were used. Wave amplitudes of 10 mm, 15 mm and 20 mm were used for periods 0.65 s to 0.8 s, 0.95 s and 1.1 s to 2 s, respectively. Larger wave amplitudes were also used for selected wave periods. The transmitted wave-field was recorded with a group of ten wave probes. The key findings of the campaign are as follows.

- Wave-energy transmission increases monotonically, as wave period increases. Wave transmission ranged from almost zero to full for the wave periods considered.

- The high-concentration array transmits less energy than the low-concentration array. However, wave-energy transmission is not a simple function of concentration for mid-range wave periods, approximately 1.1 s to 1.85 s. The lack of a simple relationship between transmission and concentration was attributed to wave-energy attenuation due to collisions between disks for the tests using a high-concentration array.

- The proportion of wave energy transmitted is strongly dependent on wave amplitude for periods less than 1 s. Doubling wave amplitudes, in this regime, caused transmitted energies to decrease by approximately 40 % and 65 % for the low- and high-concentration arrays, respectively. Reduced wave-energy transmission for large-amplitude waves and short wave periods coincided with the onset of strong wave overwash of the disks.

- The proportion of wave energy transmitted is weakly dependent on wave amplitude for mid-range wave periods and the high-concentration array. Doubling the wave amplitude for period 1.4 s caused the proportion of transmitted energy to decrease by approximately 7 %. Reduced wave-energy transmission for the large-amplitude wave, in this case, is attributed to relatively strong collisions.

Predictions of the energy transmitted by the arrays given by theoretical models were compared to transmitted energies extracted from the experimental data. The models used are based on linear, potential-flow theory to model the water, and thin-plate theory to model the disks. Wave-energy attenuation is due to an accumulation of scattering events.

The key findings of the comparison of the theoretical models and the experimental data are as follows.

- Model predictions of the transmitted energy agree with the experimental data for almost all tests using the low-concentration array. The only exception is the large-amplitude test using wave period 0.95 s, i.e. the test in which strong wave overwash of the disks occurs.

- For the high-concentration array, the theoretical models generally overestimate the proportion of wave energy transmitted. The overestimation is largest for wave periods $1.1\,\mathrm{s}$ to $1.85\,\mathrm{s}$, i.e. the tests in which collisions were strongest.

Model-data agreement for the low-concentration array and small-amplitude waves implies that in this regime:

(i) scattering is the dominant source of wave attenuation; and

(ii) linear, potential-flow/thin-plate and transport theories provide a valid model to determine wave transmission through an array of floating disks.

The pronounced loss of model accuracy for large-amplitude waves and the high-concentration array indicates other sources of wave-energy attenuation must be considered in these regimes.

The correlation found between loss of model accuracy and strong, frequent collisions between disks indicates a composite scattering/collision model is necessary for high-concentration arrays. Shen and Squire (1998) proposed a one-dimensional model of wave energy attenuation due to collisions between floating bodies, using granular-flow theory. The model was motivated by investigations of wave-induced collisions between ice floes in the ice-covered ocean (e.g. Martin and Becker, 1987; Frankenstein et al., 2001). Shen and Squire (1998) assumed wavelengths to be much greater than body diameters, and hence the bodies do not scatter waves. A modified version of the model is, therefore, required for comparison with the experiments reported here, as the incident waves are scattered by the disks.

The observed correlation between loss of model accuracy and strong overwash in the large-amplitude/short-period tests indicates models should account for the onset of overwash and wave-energy attenuation due to overwash. However, to the authors' knowledge, the overwash phenomenon is unique to wave interactions with floating, thin plates, and an overwash model does not exist at present.

Acknowledgements

References

M. Abramowitz and I. Stegun. *Handbook of mathematical functions.* Dover, 1964.

J. B. Allen and L. R. Rabiner. A unified approach to short-time Fourier analysis and synthesis. *P. IEEE*, 65:1558–1564, 1977.

L. G. Bennetts and V. A. Squire. On the calculation of an attenuation coefficient for transects of ice-covered ocean. *Proc. R. Soc. Lond. A*, 468(2137):136–162, 2012a.

L. G. Bennetts and V. A. Squire. Model sensitivity analysis of scattering-induced attenuation of ice-coupled waves. *Ocean Model.*, 45–46:1–13, 2012b.

L. G. Bennetts, M. A. Peter, V. A. Squire, and M. H. Meylan. A three-dimensional model of wave attenuation in the marginal ice zone. *J. Geophys. Res.*, 115(C12043):doi 10.1029/2009JC005982, 2010.

M. V. Berry and S. Klein. Transparent mirrors: Rays, waves and localization. *Eur. J. Phys.*, 18: 222–228, 1997.

L. C. Botten, T. P. White, A. A. Asatryan, T. N. Langtry, C. M. de Sterke, and R. C. McPhedran. Bloch mode scattering matrix methods for modeling extended photonic crystal structures. I. Theory. *Phys. Rev. E*, 70:056606, 2004.

L. Cohen. Time-frequency distributions - a review. *P. IEEE*, 77:941–981, 1989.

M. J. Doble and J.-R. Bidlot. Wavebuoy measurements at the Antarctic sea ice edge compared with an enhanced ECMWF WAM: progress towards global waves-in-ice modeling. *Ocean Model.*, 70: 166–173, 2013.

R. Eatock-Taylor. Hydroelastic analysis of plates and some approximations. *J. Eng. Math.*, 58: 267–278, 2007.

L. L. Foldy. The multiple scattering of waves. I. General theory of isotropic scattering by randomly distributed scatterers. *Phys. Rev.*, 67:107–119, 1945.

S. Frankenstein, S. Loset, and H. H. Shen. Wave-ice interactions in Barents Sea marginal ice zone. *J. Cold Reg. Eng.*, 15(2):91–102, 2001.

I. D. Howells. The multiple scattering of waves by weak random irregularities in the medium. *Proc. R. Soc. Lond. A*, 252:431–462, 1960.

M. Isaacson. Fixed and floating axisymmetric structures in waves. *J. Waterw. Port. Coastal and Ocean Div.*, pages 180–199, 1982.

A. Ishimaru. *Wave propagation and scattering in random media.* Academic Press Inc., 1978.

J. B. Keller. Gravity waves on ice-covered water. *J. Geophys. Res.*, 103(C4):7663–7669, 1998.

A. L. Kohout and M. H. Meylan. An elastic plate model for wave attenuation and ice floe breaking in the marginal ice zone. *J. Geophys. Res.*, 113(C09016):doi 10.1029/2007JC004434, 2008.

C. M. Linton and P. McIver. *Mathematical techniques for wave/structure interactions.* Chapman & Hall/CRC, 2001.

P. A. Martin. *Multiple scattering: interaction of time-harmonic waves with N obstacles.* Cambridge University Press, 2006.

S. Martin and P. Becker. High-frequency ice floe collisions in the Greenland Sea during the 1984 marginal ice zone experiment. *J. Geophys. Res.*, 92(C7):7071–7084, 1987.

D. Masson and P. LeBlond. Spectral evolution of wind-generated surface gravity waves in a dispersed ice field. *J. Fluid Mech.*, 202:111–136, 1989.

M. H. Meylan and D. Masson. A linear Boltzmann equation to model wave scattering in the marginal ice zone. *Ocean Model.*, 11:417–427, 2006.

M. H. Meylan and V. A. Squire. The response of ice floes to ocean waves. *J. Geophys. Res.*, 99(C1): 891–900, 1994.

M. H. Meylan and V. A. Squire. Response of a circular ice floe to ocean waves. *J. Geophys. Res.*, 101: 8869–8884, 1996.

M. H. Meylan, V. A. Squire, and C. Fox. Towards realism in modeling ocean wave behavior in marginal ice zones. *J. Geophys. Res.*, 102(C10):22981–22991, 1997.

F. Montiel, L. G. Bennetts, V. A. Squire, F. Bonnefoy, and P. Ferrant. Hydroelastic response of floating elastic disks to regular waves. Part 2: Modal analysis. *J. Fluid Mech.*, 723:629–652, 2013a.

F. Montiel, F. Bonnefoy, P. Ferrant, L. G. Bennetts, V. A. Squire, and P. Marsault. Hydroelastic response of floating elastic disks to regular waves. Part 1: Wave tank experiments. *J. Fluid Mech.*, 723:604–628, 2013b.

W. Perrie and Y. Hu. Air-ice-ocean momentum exchange. Part 1: Energy transfer between waves and ice floes. *J. Phys. Oceangr.*, 26:1705–1720, 1996.

M. A. Peter and M. H. Meylan. Infinite depth interaction theory for arbitrary floating bodies applied to wave forcing of ice floes. *J. Fluid Mech.*, 500:145–167, 2004.

H. H. Shen and V. A. Squire. Wave Damping in Compact Pancake Ice Fields Due to Interactions Between Pancakes, In M. O. Jeffries, editor, *Antarctic Sea Ice: Physical Processes, Interactions and Variability*, pages 325–342. AGU Antarctic Research Series 74. American Geophysical Union, 1998.

V. A. Squire and S. C. Moore. Direct measurement of the attenuation of ocean waves by pack ice. *Nature*, 283:365–368, 1980.

J. J. Stoker. *Water Waves: The Mathematical Theory with Applications*. Interscience, New York, 1957.

P. Wadhams. *The effect of a sea ice cover on ocean surface waves*. PhD thesis, Scott Polar Research Institute, University of Cambridge, Cambridge, U.K., 1973.

P. Wadhams. The seasonal ice zone. In N. Untersteiner, editor, *The Geophysics of Sea Ice*, pages 825–991. Plenum, New York, 1986.

P. Wadhams, V. A. Squire, D. J. Goodman, A. M. Cowan, and S. C. Moore. The attenuation rates of ocean waves in the marginal ice zone. *J. Geophys. Res.*, 93(C6):6799–6818, 1988.

R. Wang and H. Shen. Gravity waves propagating into an ice-covered ocean: A viscoelastic model. *J. Geophys. Res.*, 115(C06024):doi 10.1029/2009JC005591, 2010.

J. E. Weber. Wave attenuation and wave drift in the marginal ice zone. *J. Phys. Oceangr.*, 17: 2351–2361, 1987.

T. D. Williams, L. G. Bennetts, D. Dumont, V. A. Squire, and L. Bertino. Wave-ice interactions in the marginal ice zone. Part 1: Theoretical foundations. *Ocean Model.*, 71:81–91, 2013a.

T. D. Williams, L. G. Bennetts, D. Dumont, V. A. Squire, and L. Bertino. Wave-ice interactions in the marginal ice zone. Part 2: Numerical implementation and sensitivity studies along 1d transects of the ocean surface. *Ocean Model.*, 71:92–101, 2013b.